AIAA JOURNAL
Vol. 45, No. 7, July 2007

Flutter-Boundary Identification for Time-Domain Computational Aeroelasticity

Jack J. McNamara* and Peretz P. Friedmann†
University of Michigan, Ann Arbor, Michigan 48109

DOI: 10.2514/1.26706

Three time-domain damping/frequency/flutter identification techniques are discussed; namely, the moving-block approach, the least-squares curve-fitting method, and a system-identification technique using an autoregressive moving-average model of the aeroelastic system. These methods are evaluated for use with time-intensive computational aeroelastic simulations, represented by the aeroelastic transient responses of a double-wedge airfoil and three-dimensional wing in hypersonic flow. The responses are generated using the NASA Langley CFL3D computational aeroelastic code, in which the aerodynamic loads are computed from the unsteady Navier–Stokes equations. In general, the methods agree well. The system-identification technique, however, provided quick damping and frequency estimates with minimal response-record length. In the present case, the computational cost required to generate each aeroelastic transient was reduced by 75%. Finally, a flutter margin for discrete-time systems, constructed using the autoregressive moving-average approach, is evaluated for use in the hypersonic flow regime for the first time. For the binary-mode case, the flutter margin exhibited a linear correlation with dynamic pressure, minimizing the number of responses required to locate flutter. However, the flutter margin was not linear for the multimode system, indicating that it does not perform as expected in all cases.

Nomenclature

A_i	=	constant in sinusoidal representation of transient modal amplitude
$\bar{A}_i$	=	coefficients of discrete-time characteristic equation
$\{\mathbf{A_p}\}$	=	estimated aeroelastic system matrix
a	=	nondimensional offset between the elastic axis and the midchord, positive for the elastic axis behind the midchord
a_o, a_i, b_i	=	coefficients used for damping and frequency identification
b	=	semichord
$\{\mathbf{C_p}\}$	=	estimated aeroelastic system matrix
c	=	reference-length chord length of the double-wedge airfoil
E	=	squared error between the curve fit and actual data
F_N	=	multimode flutter-prediction parameter
F_Z	=	two-mode flutter-prediction parameter
$F^-(j)$	=	intermediate function used to compute the flutter-prediction parameter
f	=	exponential function for curve fit
$G(z_d)$	=	characteristic polynomial
h	=	airfoil vertical displacement at the elastic axis
h_i	=	states in state-space representation of the autoregressive model
I_α	=	mass moment of inertia about the elastic axis
K_α, K_h	=	spring constants in pitch and plunge ($I_\alpha\omega_\alpha^2$ and $m\omega_h^2$), respectively
k	=	discrete time
M	=	freestream Mach number
M_f	=	flutter Mach number
$\mathbf{M}$, $\mathbf{K}$	=	generalized mass and stiffness matrices of the structure
m	=	mass per unit span
N	=	number of points in the response signal
N_b	=	number of points in the moving-block number
n_m	=	number of modes
p	=	pressure
$\mathbf{Q}$	=	generalized force vector for the structure
Q_i	=	generalized force corresponding to mode i
Q_i'	=	finite Fourier transform of the transient of mode i
$\bar{Q}_i'$	=	amplitude of the Fourier spectrum at one time step (moving-block function)
q_f	=	dynamic pressure at flutter
q_i	=	modal amplitude of mode i
q_∞	=	dynamic pressure
Re	=	Reynolds number
r	=	real part of the eigenvalue
r_α	=	nondimensional radius of gyration
S	=	surface area of the structure
S_α	=	static mass moment of the wing section about the elastic axis
s	=	imaginary part of the eigenvalue
T_E	=	kinetic energy of the structure
T_e	=	sample time
T_r	=	response-signal length
t	=	time
t_k	=	kth point in discrete time
U_E	=	potential energy of the structure
V	=	freestream velocity
v_n	=	normal velocity of the airfoil surfaces
w	=	displacement of the surface of the structure
$\bar{X}_j$, $\bar{Y}_j$	=	flutter-parameter matrices
$\{X_p\}$	=	state matrix
x, y, z	=	spatial coordinates
x_α	=	nondimensional offset between the elastic axis and the cross-sectional center of gravity, positive for the center of gravity behind the elastic axis
z_d	=	complex variable used in the discrete-time system, $z_d^{-1}qk = q_{k-1}$
α	=	airfoil pitch displacement about the elastic axis
α_s	=	static angle of attack
γ	=	ratio of specific heats
Δt	=	time step

Received 26 July 2006; revision received 28 February 2007; accepted for publication 26 March 2007.

*Post-Doctoral Scholar, Department of Aerospace Engineering; currently Assistant Professor, Aerospace Engineering Department, Ohio State University, Columbus, OH. Member AIAA.

†François-Xavier Bagnoud Professor, Department of Aerospace Engineering. Fellow AIAA.

δ_{k-1} = input for the ARMA model of the aeroelastic system
ζ = damping ratio
Λ = estimated matrix eigenvalue
μ_m = mass ratio
ρ = air density
τ = thickness ratio
τ_t = time
$\mathbf{\Phi}$ = modal matrix
ϕ_i = mode shape for mode i
ϕ_{ai} = phase angle of modal amplitude history in sinusoidal representation for mode i, rad
ω_α, ω_h = natural frequencies of uncoupled pitch and plunge motions
ω_i = frequency of mode i
ω_{ni} = natural frequency of mode i
(), () = first and second derivatives with respect to time

I. Introduction

ADVANCED aircraft design is a multidisciplinary task that combines stress analysis, structural dynamics, steady/unsteady aerodynamics, flight-control mechanics, and, at high speed, heat transfer. Advances in computer technology, computational fluid dynamics (CFD), and computational aeroelasticity (CAE) are systematically reducing the amount of expensive experimental testing necessary in aircraft design. In extreme cases such as the hypersonic flow environment, CFD-based CAE tools are essential for vehicle design, due to a lack of experimental facilities and techniques [1]. In such cases, the CAE analysis is carried out in the time domain by coupling CFD with the structural analysis. Hence, flutter-boundary identification requires system-stability computations based on a series of transient aeroelastic responses. The computational cost of such a procedure is directly related to both the amount of response time required to accurately estimate system damping and frequencies and the number of responses required to locate the flutter point.

Several methods for time-domain damping/frequency and flutter-boundary identification are available [2–17]. In [12], three methods were compared: the moving-block approach (MBA) [3–6], the least-squares curve-fitting method (LSCFM) [7], and a system-identification approach using an autoregressive moving-average (ARMA) model [8–15]. The ARMA approach was found to be superior because it required smaller time records and therefore could reduce the cost of CFD-based CAE simulations.

The objective of this paper is to further evaluate the ARMA method, specifically, in the context of reducing the cost of time-intensive CAE solutions. This is accomplished by comparing damping, frequency, and flutter-boundary estimates computed with the MBA, LSCFM, and ARMA methods. The aeroelastic response data required for this comparison is computed by solving the unsteady Navier–Stokes equations for two configurations operating in hypersonic flow: 1) a two-degree-of-freedom double-wedge airfoil and 2) a low-aspect-ratio wing.

A. Summary of Methods

To provide a basic understanding of the identification methods used in this study, each is briefly described next.

1. Moving-Block Approach

The MBA approach, developed in the 1970s by the Lockheed-California Company, is based on a fast Fourier transformation (FFT) and has been widely used within the rotorcraft industry [4]. Consider a transient signal,

$$q_i(t) = A_i e^{-\zeta_i \omega_{ni} t} \sin(\omega_i t + \phi_{ai}) \tag{1}$$

where

$$\omega_i^2 = \omega_{ni}^2 (1 - \zeta_i^2) \tag{2}$$

The finite Fourier transform of this signal is

$$Q_i'(\omega_i, \tau_t) = \int_{\tau_t}^{\tau_t + T_r} A_i e^{-\zeta_i \omega_{ni} t} \sin(\omega_i t + \phi_{ai}) e^{-i\omega_i t} dt \tag{3}$$

where $Q_i'(\omega_i, \tau_t)$ is a function of τ_t at the analysis frequency ω_i. The moving-block function is defined as the amplitude of Eq. (3). For small damping (i.e., $\zeta_i \ll 1$), the natural logarithm of the moving-block function is

$$\ell_n \bar{Q}_i'(\omega_i, \tau_t) = -\zeta_i \omega_i \tau_t + \tfrac{1}{2}\zeta_i \sin\{2(\omega_i \tau_t + \phi_{ai})\} + \text{constant} \tag{4}$$

Note that the right-hand side of Eq. (4) has a linear component with a slope of $-\zeta_i \omega_i$ and an oscillatory component at twice the analysis frequency ω_i.

When using this method, an analysis frequency of interest is selected by computing the frequency spectrum of the entire transient response using a FFT algorithm. Next, the left-hand side of Eq. (4) is calculated on the first block of the data, in which $N_b < N$ at $\tau_t = 0$. This is repeated $N - N_b$ times, after shifting the block one sample point at a time (i.e., $\tau_t = n\Delta t$ for $n = 0, 1, 2, \ldots, N - N_b$). The slope of the resulting series of data points is approximated using a linear least-squares fit. The damping is evaluated by dividing this slope by the analysis frequency. Note that in this study, Goertzel's algorithm [4] was used to compute the left-hand side of Eq. (4).

A critical step in this method is the selection of an analysis frequency from the frequency spectrum of a response. If the aeroelastic response of the system consists of a set of transient modal amplitudes, $\{q_1(t), q_2(t), \ldots, q_{n_m}(t)\}$, there are two options. One option is to calculate the frequency spectrum of the response from the transient displacement of a point on the structure. In this case, the analysis frequencies of the displacement will correspond to local maxima in the frequency spectrum. Thus, image processing is required to locate the frequencies, either interactively by visual inspection or computationally using an image processing algorithm. In presenting results, this approach is designated as MBA1. The second option for locating the frequencies is to calculate the frequency spectrum of each transient modal amplitude individually. Because the modal amplitudes are coupled through the generalized forces, the frequency spectrum of each modal amplitude will contain multiple frequencies. The analysis frequencies, therefore, should be selected as the global maximum in the frequency spectrum of each modal amplitude. Note that as flutter is approached, the frequencies of certain modal amplitudes become dominant. When this occurs, some modes will appear to have sudden shifts in damping and frequency. This is due to the MBA tracking the damping and frequency characteristics of a different, dominant, mode. Although information of some of the modes is lost when this occurs, this option provides insight into the interaction between the modes as the flutter Mach number is approached. In presenting results, the second approach is designated as MBA2.

Two issues with the MBA for damping and frequency identification exist. In cases in which a particular mode damps out rapidly, the moving-block function does not form a straight line if the response record is too long [3]. Therefore, the damping, which is calculated from a linear least-squares fit of the MBA output data, will be incorrect. Because the amount of damping in each mode is not known before a response is processed, this issue introduces uncertainty in determining the appropriate record lengths for accurate damping estimates. A second issue is the inability to identify peaks in the frequency spectrum when there are closely spaced modal frequencies [3,4].

2. Least-Squares Curve-Fitting Method

The LSCFM, developed in the 1970s at the NASA Langley Research Center, solves a least-squares problem to fit exponential functions to transient data [7]. Consider the following exponential function:

$$f(t) = a_0 + \sum_{i=1}^{n_m} e^{-\zeta_i \omega_{ni} t}\{a_i \cos(\omega_i t) + b_i \sin(\omega_i t)\} \tag{5}$$

The modal damping and frequency of a transient response can be calculated by minimizing the squared-error difference between the output fit $f(t_k)$ and the input transient response $w(t_k)$, where t_k is the kth discrete-time sample of the response. This error is given by

$$E = \sum_{k=1}^{N}\{f(t_k) - w(t_k)\}^2 \tag{6}$$

This is a nonlinear least-squares problem. One method of solution is to provide initial "guess" values for ζ_i and ω_i and then solve the linear least-squares problem for a_0, a_i, and b_i. The curve fit is then calculated by searching for the ζ_i and ω_i that minimize Eq. (6). At each search step, the linear coefficients a_0, a_i, and b_i are updated, and the error is recomputed using the current ζ_i and ω_i. The search for ζ_i and ω_i in this study is performed using the subroutine FMINSEARCH in MATLAB.

A shortcoming of this method is the dependence of the results on the initial values given for ζ_i and ω_i [12]. Also, the computational time required to find the linear coefficients that minimize Eq. (6) can be relatively long; particularly when more than two modes are present in the aeroelastic system.

3. *Autoregressive Moving-Average Method*

The ARMA method was first investigated by Onoda [8] for the purpose of characterizing the response of a flutter model [9]. This work was expanded in [9], in which the flutter boundary of a system was identified using the autoregressive (AR) coefficients of an ARMA model. The method was validated using the response data of a cantilever wing tested in the transonic wind tunnel for flutter tests at the National Aerospace Laboratory/NLR. It was concluded that the ARMA process, in conjunction with Jury's stability criterion [18], could accurately predict the flutter boundary from subcritical response data.

The approach used in this study is based on a single-input/single-output deterministic ARMA model of the aeroelastic system, with $2n_m$ AR coefficients and one moving-average (MA) coefficient [12]. The model has the following form:

$$w_k + \sum_{i=1}^{2n_m} a_i w_{k-i} = b_1 \delta_{k-1} \tag{7}$$

where $2n_m$ AR coefficients are used to determine the aeroelastic system damping and frequencies, and one MA coefficient is sufficient for identifying an aeroelastic static offset [12]. To identify the damping and frequency, the transient aeroelastic response is represented by the following AR model:

$$w_k + \sum_{i=1}^{2n_m} a_i w_{k-i} = 0 \tag{8}$$

This can be written in state-space form as

$$\{X_p\}_{k+1} = \{\mathbf{A_p}\}\{X_p\}_k \qquad w_k = \{\mathbf{C_p}\}\{X_p\}_k \tag{9}$$

where

$$\{\mathbf{A_p}\} = \begin{bmatrix} -a_1 & 1 & 0 & \cdots & 0 \\ -a_2 & 0 & 1 & \cdots & 0 \\ \vdots & \vdots & \vdots & \ddots & \vdots \\ -a_{2n_m-1} & 0 & 0 & \cdots & 1 \\ -a_{2n_m} & 0 & 0 & \cdots & 0 \end{bmatrix} \tag{10}$$

and

$$\{\mathbf{C_p}\} = [1 \quad 0 \quad 0 \quad \cdots \quad 0] \tag{11}$$

The state vector $\{X_p\}_k$ is defined as

$$\{X_p\}_k \equiv \begin{Bmatrix} w_k \\ h_1(k) \\ \vdots \\ h_{2n_m-1}(k) \end{Bmatrix} \tag{12}$$

with

$$\begin{gathered} w_k = -a_1 w_{k-1} + h_1(k-1) \\ h_1(k) = -a_2 w_{k-1} + h_2(k-1) \\ \vdots \\ h_{2n_m-2}(k) = -a_{2n_m-1} w_{k-1} + h_{2n_m-1}(k-1) \\ h_{2n_m-1}(k) = -a_{2n_m} w_{k-1} \end{gathered} \tag{13}$$

The state-space description of the AR model in Eq. (9) is in observer form and is completely observable. The aeroelastic system damping and frequencies are determined from the eigenvalues of the estimated matrix $\{\mathbf{A_p}\}$, given in Eq. (10) [12]. These can be written as

$$\Lambda_j = r_j + i s_j \qquad \Lambda_{j+n_m} = r_j - i s_j \tag{14}$$

where $j = 1, 2, \cdots, n_m$. Note that the AR model is in the discrete-time domain, therefore, the aeroelastic modal damping and frequencies in the continuous-time domain are given by [12]

$$\zeta_j = \frac{1}{2T_e}\log_e(r_j^2 + s_j^2) \qquad \omega_j = \frac{1}{T_e}\tan^{-1}\frac{s_j}{r_j} \tag{15}$$

In this study, the AR coefficients are determined from the aeroelastic responses using the subroutine AR from the system-identification toolbox in MATLAB. The sampling times used to calculate the AR coefficients from the response data are

$$T_e = \frac{\pi}{2(\omega_n)_{\max}} \tag{16}$$

where $(\omega_n)_{\max}$ is the maximum system natural frequency in radians/second.

Recently, a procedure for finding the flutter margin of discrete-time systems (FMDS) using the AR coefficients of an ARMA model has been developed [13–15]. For binary flutter problems, the flutter margin provides equivalent results to the Zimmerman and Weissenburger [2] flutter margin of continuous-time systems [13]. Furthermore, it has been shown to provide a linear correlation with dynamic pressure for $0.4q_f < q_\infty < 1.0q_f$, in both the subsonic [13–15] and supersonic [13] flow regimes. This is in contrast to system damping that has a nonlinear variation with dynamic pressure and often changes abruptly near the flutter point. From a computational aeroelasticity perspective, a linear flutter margin minimizes the number of subcritical responses required to locate the flutter boundary.

Consider the characteristic polynomial consisting of the AR coefficients from the ARMA model [13]

$$G(z_d) = z_d^{2n_m} + a_1 z_d^{2n_m-1} + \cdots + a_{2n_m-1} z_d + a_{2n_m} \tag{17}$$

that can be rewritten as

$$G(z_d) = \bar{A}_{2n_m} z_d^{2n_m} + \bar{A}_{2n_m-1} z_d^{2n_m-1} + \cdots + \bar{A}_1 z_d + \bar{A}_0 \tag{18}$$

where

$$\begin{Bmatrix} \bar{A}_{2n_m} \\ \bar{A}_{2n_m-1} \\ \vdots \\ \bar{A}_0 \end{Bmatrix} = \begin{Bmatrix} 1 \\ a_1 \\ \vdots \\ a_{2n_m} \end{Bmatrix} \tag{19}$$

For a bending-torsion aeroelastic system ($n_m = 2$), the flutter parameter is given as [13]

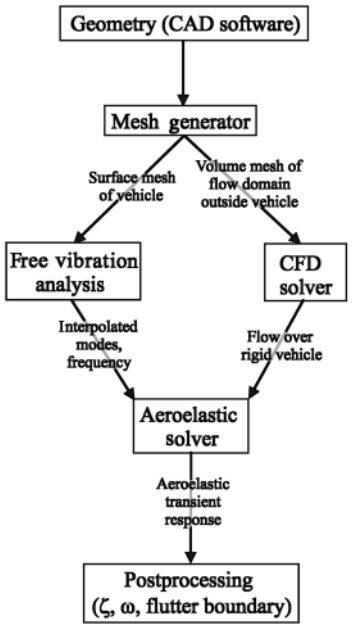

Fig. 1 Flow diagram of the computational aeroelastic solution procedure.

$$F_Z = \frac{F^-(2n_m - 1)}{F^-(2n_m - 3)^2} = \frac{F^-(3)}{F^-(1)^2} \tag{20}$$

where

$$F^-(j) = \det(X_j - Y_j) \tag{21}$$

and

$$\{X_j\} = \begin{bmatrix} \bar{A}_{2n_m} & \cdots & \bar{A}_{2n_m-j+1} \\ 0 & \ddots & \vdots \\ 0 & 0 & \bar{A}_{2n_m} \end{bmatrix}, \quad \{Y_j\} = \begin{bmatrix} \bar{A}_{j-1} & \cdots & \bar{A}_0 \\ \vdots & \ddots & 0 \\ \bar{A}_0 & 0 & 0 \end{bmatrix} \tag{22}$$

In a follow-up study [14], the multimode version of the flutter parameter is proposed as

$$F_N = \frac{F^-(2n_m - 1)}{F^-(2n_m - 2)^2} \tag{23}$$

It is interesting to note that Eqs. (20) and (23) are not equal for $n_m = 2$. Furthermore, a mathematical foundation for Eq. (23) is not provided in [14], nor is this discrepancy addressed in detail. However, the multimode parameter was demonstrated to vary linearly with dynamic pressure, using both computational and wind-tunnel aeroelastic flutter data, in the subsonic flow regime.

II. Calculation of Transient Aeroelastic Responses

The solution of the unsteady Navier–Stokes equations represents an extreme case in terms of computational cost. Thus, using an approach based on the solution of the Navier–Stokes equations represents an excellent test case for evaluating the ARMA method. Recently, the authors of this paper were involved in a number of fundamental studies on the hypersonic aeroelastic behavior of generic reusable launch vehicles [1,19–25]. The NASA Langley CFL3D code [26,27] used extensively in these studies contains both a CFD Navier–Stokes solver and a deforming-mesh capability enabling aeroelastic computations. Therefore, it is an ideal tool for generating hypersonic aeroelastic response data required for the present study.

A. Euler/Navier–Stokes Solver in CFL3D

The CFL3D code uses an implicit finite volume algorithm based on upwind-biased spatial differencing to solve both the time-dependent Euler equations and Reynolds-averaged Navier–Stokes equations. Multigrid and mesh-sequencing are available for convergence acceleration. The algorithm, which is based on a cell-centered scheme, uses upwind-differencing based on either flux-vector splitting or flux-difference splitting and can sharply capture shock waves. For applications using the thin-layer Navier–Stokes equations, different turbulence models are available. For time-accurate problems using a deforming mesh, an additional term accounting for the change in cell volume is included in the time discretization of the governing equations [28]. Because CFL3D is an implicit code using approximate factorization, linearization and factorization errors are introduced at every time step. Hence, intermediate calculations referred to as "subiterations" are used to reduce these errors. Increasing these subiterations improves the accuracy of the simulation, albeit at increased computational cost.

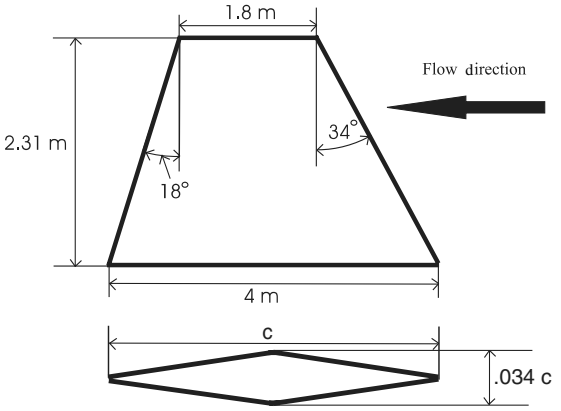

Fig. 2 Planform and cross-sectional views of the low-aspect-ratio wing.

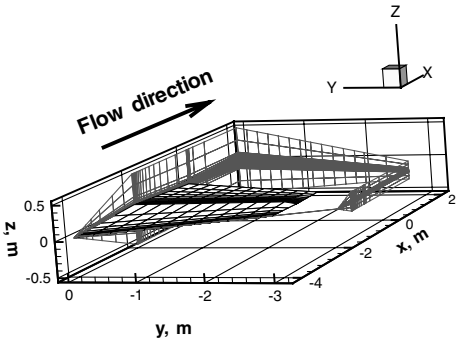

Fig. 3 Computational domain of the low-aspect-ratio wing.

B. Aeroelastic Option in CFL3D

The aeroelastic approach underlying the CFL3D code is similar to that described in [29,30]. The equations are derived by assuming that the general motion $w(x, y, z, t)$ of the structure is described by a finite modal series given by Eq. (24). The functions $\phi_i(x, y, z)$ represent the free-vibration modes of a structure:

$$w(x, y, z, t) = \sum_{i=1}^{n_m} q_i(t)\phi_i(x, y, z) \tag{24}$$

Table 1 Comparison of the Lockheed F-104 Starfighter wing with the low-aspect-ratio wing model

Parameter	F-104	Model
Wing mass, Kg	350.28	350.05
First bending frequency, Hz	13.40	13.41
First torsional frequency, Hz	37.60	37.51

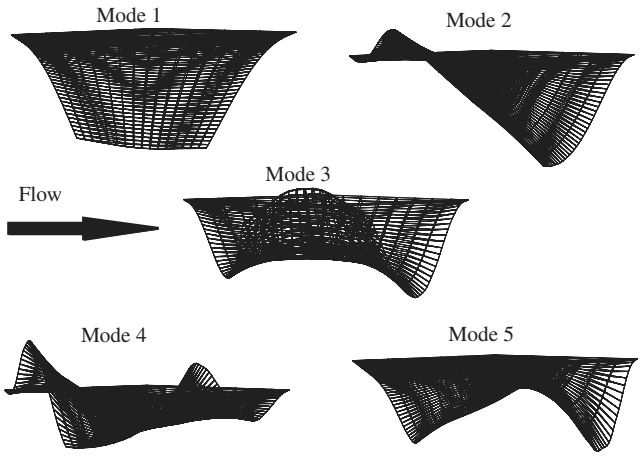

Fig. 4 First five free-vibration modes of the low-aspect-ratio wing.

The aeroelastic equations of motion are obtained from Lagrange's equations:

$$\frac{\mathrm{d}}{\mathrm{d}t}\left(\frac{\partial T_E}{\partial \dot{q}_i}\right) - \frac{\partial T_E}{\partial q_i} + \frac{\partial U_E}{\partial q_i} = Q_i, \qquad i = 1, 2, \ldots, n_m \tag{25}$$

which yield

$$\mathbf{M}\,\ddot{\mathbf{q}} + \mathbf{K}\mathbf{q} = \mathbf{Q}(\mathbf{q}, \dot{\mathbf{q}}, \ddot{\mathbf{q}}), \qquad \mathbf{q}^T = [q_1 q_2 \ldots q_{n_m}] \tag{26}$$

where the elements of the generalized force vector are given by

$$Q_i = \frac{\rho V^2}{2} c^2 \int_S \phi_i \frac{\Delta p(\mathbf{q}, \dot{\mathbf{q}}, \ddot{\mathbf{q}})\,\mathrm{d}S}{\rho V^2/2c^2} \tag{27}$$

The aeroelastic equations are written in terms of a linear state-space equation (using a state vector of the form $\{q_1(t), \dot{q}_1(t), q_2(t), \dot{q}_2(t), \ldots, q_n m(t), \dot{q}_n m(t)\}^T$) such that a modified state-transition-matrix integrator can be used to march the coupled fluid-structural system forward in time. At the beginning of each time step, the incremental structural deflections are calculated using the modal velocities and generalized aerodynamic forces. Using a deforming mesh, the mesh points are moved so that the inner mesh boundaries conform to the new deformed shape of the structure and the far-field boundaries are held stationary. The fluid equations, including the geometric conservation-law terms, compute the flowfield throughout the updated mesh. The generalized aerodynamic forces acting on the structure through the next time step are then computed. Thus, a tight coupling of the flow and the structure is implemented through the generalized aerodynamic forces. This process yields a time history of the modal displacements, modal velocities, and generalized forces.

Table 2 First five natural frequencies of the low-aspect-ratio-wing structural model

Mode number	Mode type	Frequency, Hz
1	First bending	13.41
2	First torsion	37.51
3	Second bending	49.18
4	Second torsional	77.14
5	Third torsional	79.48

Table 3 Parameters describing the double-wedge airfoil

c, m	2.35
τ	0.0336
m, kg/m	94.2
r_α	0.484
ω_h, Hz	13.4
ω_α, Hz	37.6
x_α	0.2
a	0.1

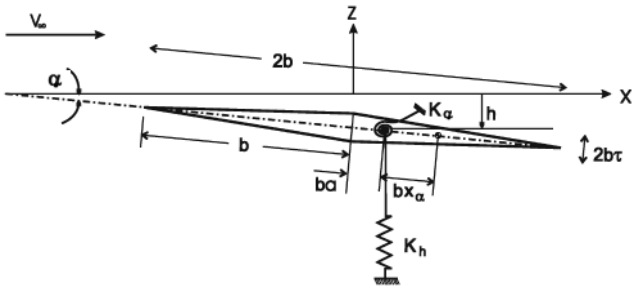

Fig. 5 Two-degree-of-freedom typical airfoil geometry.

C. Overview of the Solution Process

The general CAE solution procedure used in the present study to generate the aeroelastic transients is graphically depicted in Fig. 1. Note that this is the same procedure implemented in [19–25]. First, the vehicle geometry is created using CAD software, and from this geometry, a mesh generator is used to create a structured mesh for the flow domain around the body. Subsequently, the fluid mesh is used to compute the flow around the rigid vehicle using the CFD solver in CFL3D. In parallel, the free-vibration modes and frequencies of the structure are determined.

Using the flow solution around the rigid geometry as an initial condition, and the modal data as additional input, an aeroelastic equilibrium state is obtained for the flexible vehicle. For a geometry with vertical symmetry at zero angle-of-attack, such as those

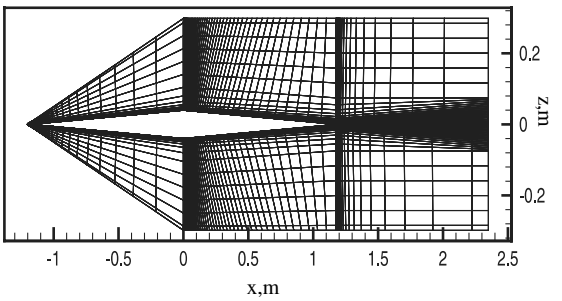

Fig. 6 Computational domain of the double-wedge airfoil.

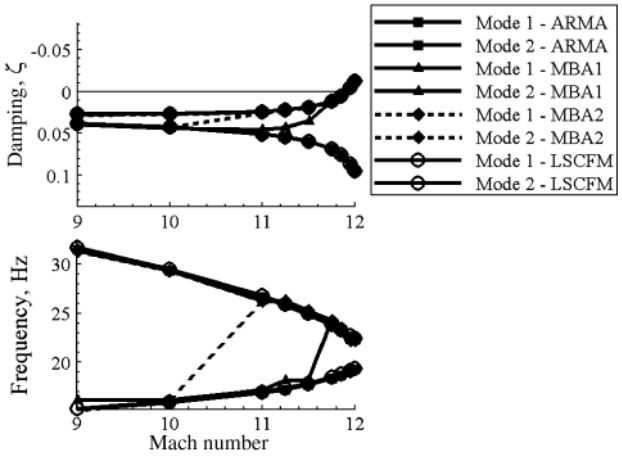

Fig. 7 Aeroelastic behavior represented by damping and frequency for a typical section using Navier–Stokes aerodynamics at 40,000 ft; predicted using different time-domain-identification techniques.

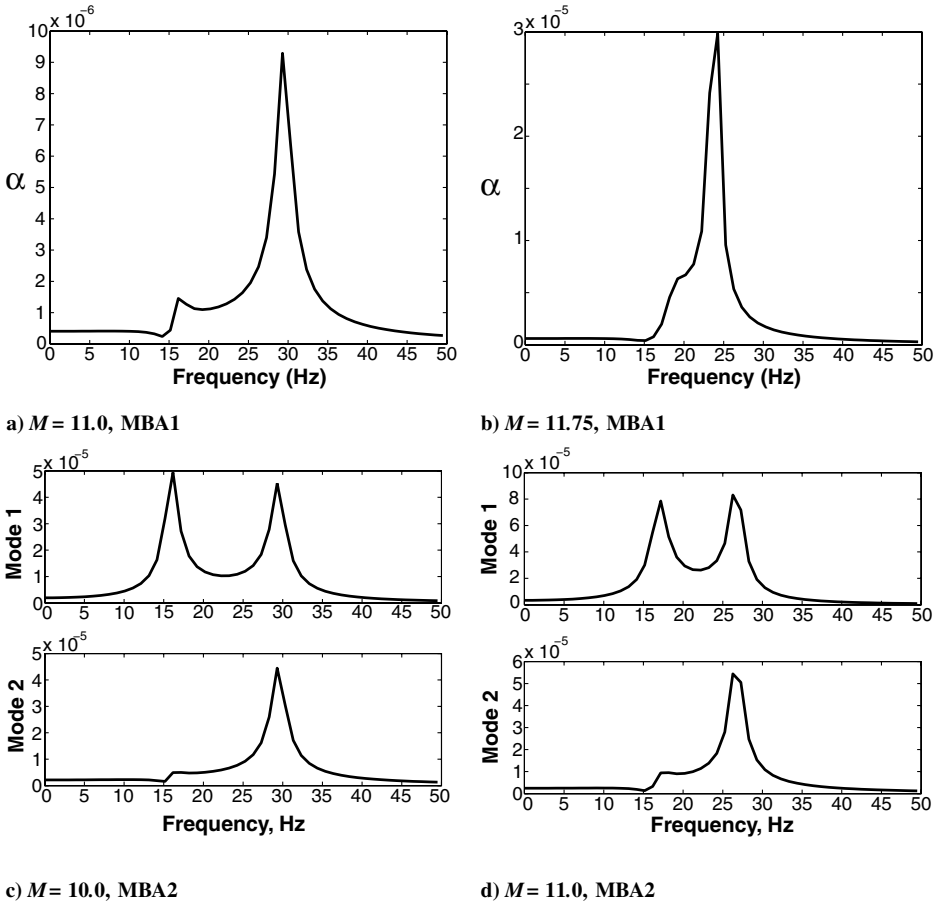

a) $M = 11.0$, MBA1 b) $M = 11.75$, MBA1

c) $M = 10.0$, MBA2 d) $M = 11.0$, MBA2

Fig. 8 Power spectrum plots of the pitch response (MBA1) and modal amplitudes (MBA2) of a typical section at 40,000 ft.

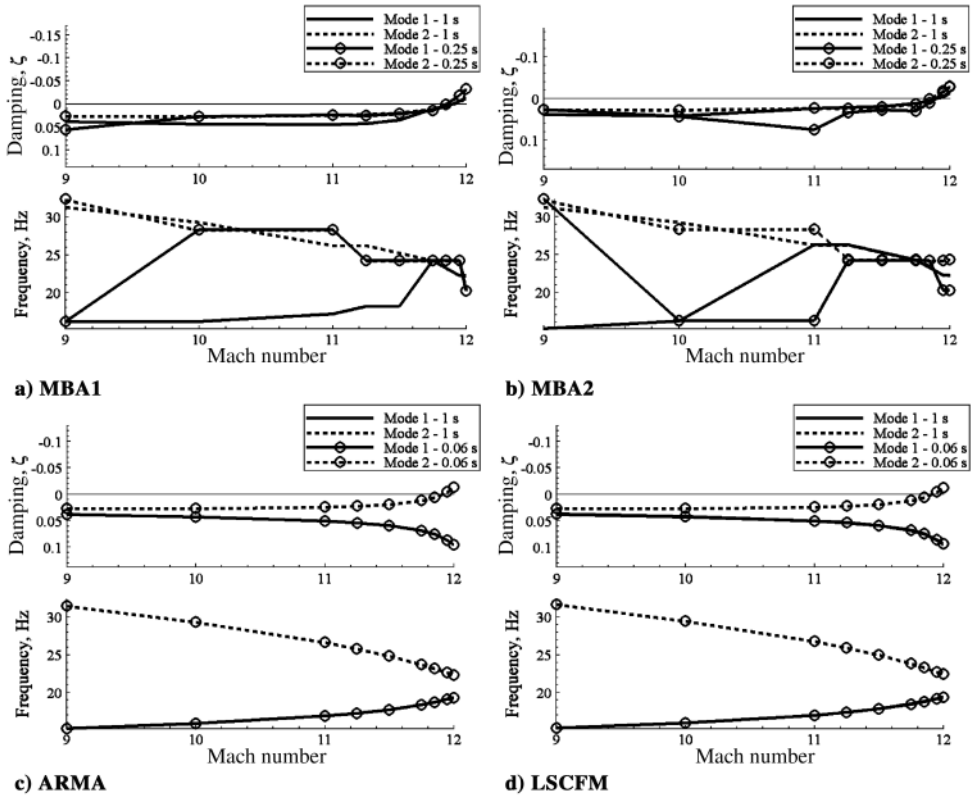

Fig. 9 Aeroelastic behavior, of a typical section using Navier–Stokes aerodynamics, predicted using different identification approaches and different time record lengths of the response.

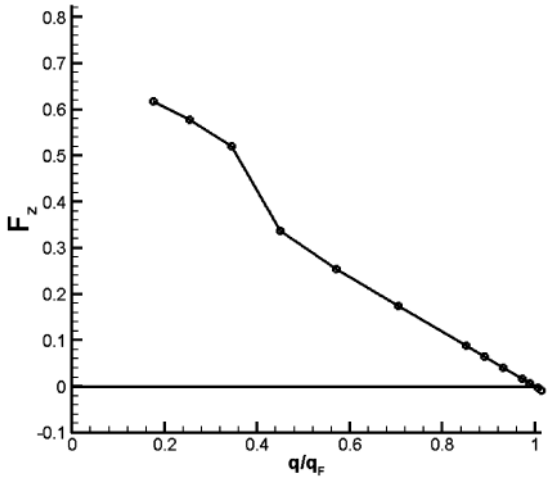

Fig. 10 Flutter margin (FMDS) for a typical section using Navier–Stokes aerodynamics at 40,000 ft.

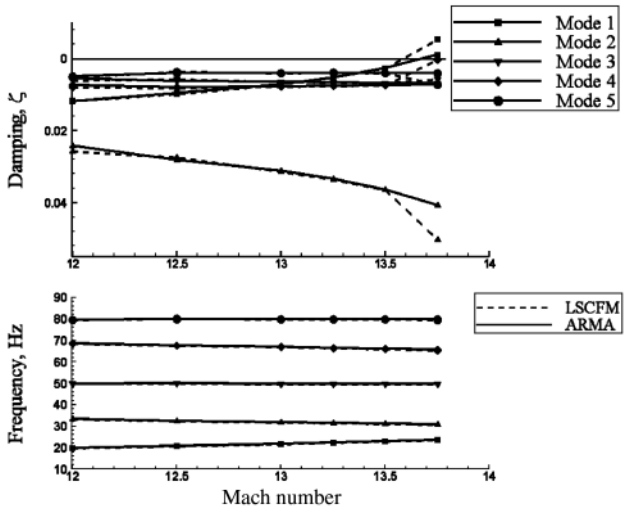

Fig. 11 Aeroelastic behavior represented by damping and frequency for a low-aspect-ratio wing using Navier–Stokes aerodynamics at 40,000 ft; predicted using the ARMA and LSCFM approaches (solid lines correspond to the ARMA results and dashed lines correspond to the LSCFM).

considered in this study, the equilibrium state is the same as the rigid state. Next, the structure is perturbed in one or more of its modes by an initial modal velocity condition, and the transient response of the structure is obtained. To determine the flutter conditions at a given altitude, aeroelastic transients are computed at several Mach numbers and the corresponding dynamic pressures. The frequency and damping characteristics are then calculated using each of the identification methods. This approach applied at the same altitude and vehicle configuration for a range of Mach numbers results in a series of damping values for the system. The flutter Mach number can be estimated from this series by interpolating the damping data points to identify the value of the Mach number at which the damping is zero.

D. Computational Model for the Low-Aspect-Ratio Wing

The three-dimensional low-aspect-ratio wing configuration used in this study is shown in Fig. 2. Note that it is representative of a fin or control surface on a hypersonic vehicle. The flow domain for the wing, shown in Fig. 3, was developed from a study [24] of grid configurations, in which the appropriate computational domain and mesh resolution required for the hypersonic aeroelastic analysis of the low-aspect-ratio wing were determined. In [24], cell distribution and grid resolution were varied to construct a grid for the hypersonic flow regime that accurately and efficiently captured the flow. Each span section plane of the flow domain extends one half-chord length downstream. The boundary of the grid surrounding the wing from the leading edge to midchord extends to a distance 10% beyond the shock that forms at $M = 5.0$. The flow domain in the spanwise direction also extends beyond the tip of the wing by 35% of the semispan length. Furthermore, the grid is tapered in all three dimensions to be compatible with the geometric taper of the wing. With 0.63×10^6 cells, this grid is a $57 \times 353 \times 33$ C-H-grid with 353 points around the wing and its wake (289 points on the wing surface), 57 points extending spanwise from the root (49 points on the wing surface), and 33 points extending radially outward from the surface.

Table 4 L_∞ norm of the error between the actual transient data and approximate curve fit using the ARMA and LSCFM approaches

Mach number	ARMA	LSCFM
12.0	0.0079	0.0083
12.5	0.0004	0.0176
13.0	0.0003	0.0095
13.25	0.0003	0.0151
13.5	0.0004	0.0135
13.75	0.0004	0.0351

The structural model for the low-aspect-ratio wing is based on the Lockheed F-104 Starfighter wing. It was developed with finite elements in MSC.NASTRAN by matching its total mass and first-bending and torsional frequencies to the corresponding F-104 wing values. A comparison of the model values with the F-104 wing is provided in Table 1. The first five modes of the structural model are shown in Fig. 4, and the corresponding natural frequencies are provided in Table 2. Note that the wing structure was assumed to be made from 2024-T3 aluminum alloy.

E. Computational Domain for the Double-Wedge Typical Section

The double-wedge airfoil model shown in Fig. 5 is considered as a typical section of the low-aspect-ratio wing described earlier. The parameters describing this configuration are listed in Table 3. The natural frequencies and mode shapes for the model were computed using the following free-vibration equations of motion [31]:

$$m\ddot{h} + S_\alpha \ddot{\alpha} + K_h h = 0 \qquad S_\alpha \ddot{h} + I_\alpha \ddot{\alpha} + K_\alpha \alpha = 0 \tag{28}$$

The CFD domain shown in Fig. 6 was extracted from the 75% span section of the mesh wrapped around the low aspect ratio described earlier. This grid is a $2 \times 705 \times 65$ C-grid with 705 points around the airfoil and its wake (577 points on the airfoil surface), one point extending spanwise one unit length to close the control volume, and 65 points extending radially outward from the surface.

III. Comparison of Methods Using the Typical Section Airfoil

The aeroelastic transient responses for the typical section airfoil were calculated at an altitude of 40,000 ft for 4000 time steps (1 s of response). Note that the chosen altitude does not represent a situation in which hypersonic flight is feasible. However, as is typical of a hypersonic aeroelastic analysis that neglects aerodynamic heating [1], this altitude was required to generate flutter at moderate Mach numbers (i.e., less than 15).

A comparison of the various methods is given in Fig. 7. Note that the aeroelastic transient responses are output from CFL3D as a vector of modal amplitudes, $\{q_1(t), q_2(t), \cdots, q_{n_m}(t)\}$. For the results labeled ARMA, MBA1, and LSCFM, the damping and frequency of the system was calculated from the pitch response of the airfoil, where

$$\begin{Bmatrix} h(t) \\ \alpha(t) \end{Bmatrix} = [\Phi] \begin{Bmatrix} q_1(t) \\ q_2(t) \end{Bmatrix} \tag{29}$$

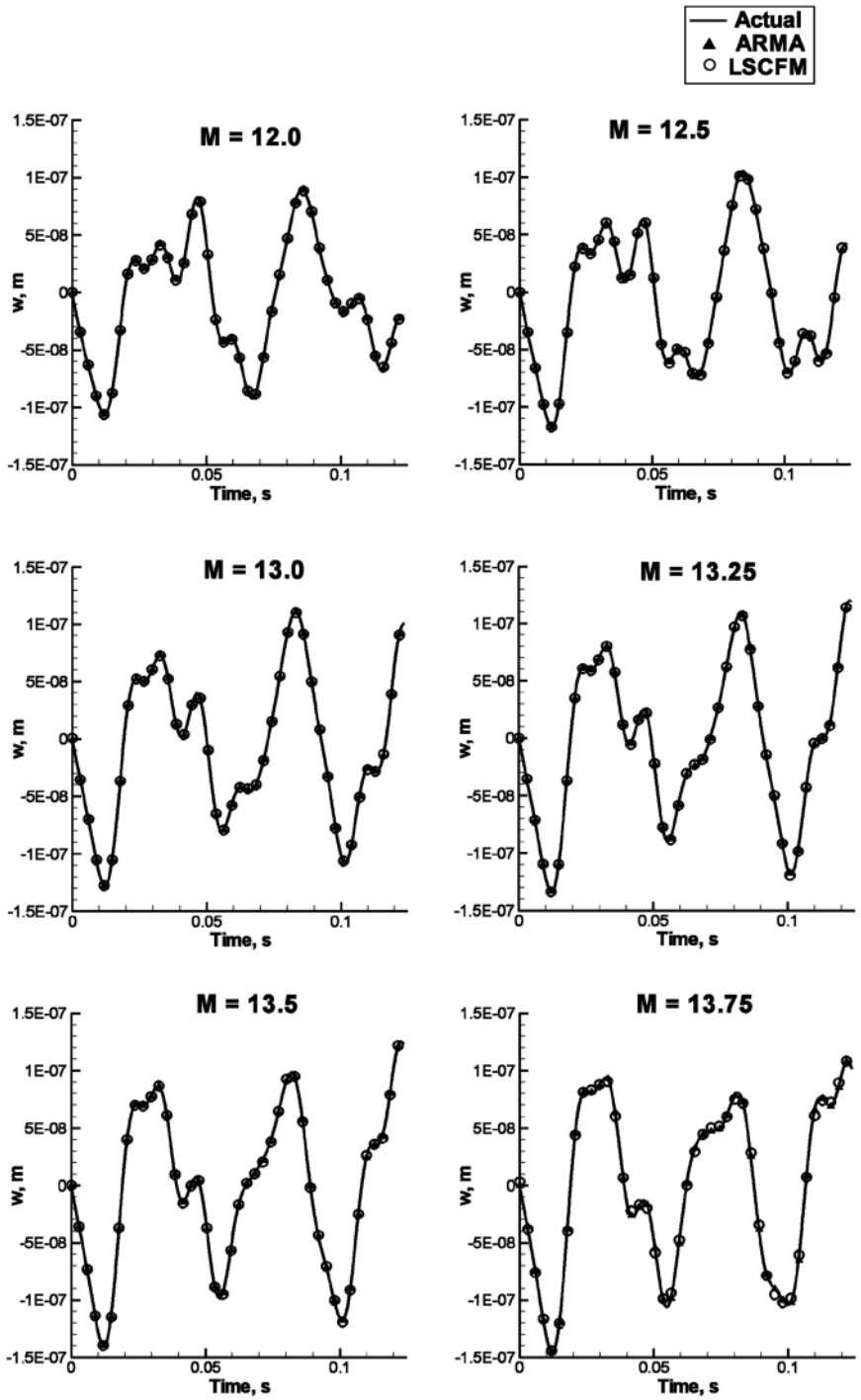

Fig. 12 Comparison of the curve fits for the displacement of a point at the leading edge of the wing tip, generated using the ARMA and LSCFM approaches.

The results labeled MBA2 were generated using the individual aeroelastic transients (i.e., $\{q_1(t), q_2(t)\}$). Thus, for the MBA1 results, analysis frequencies were selected using the MATLAB image-processing subroutine IMREGIAONALMAX to locate local maxima from the frequency spectrum of the pitch response. For the MBA2 results, the analysis frequencies were set to the global maximum of the frequency spectrum for each individual transient.

It is evident from Fig. 7 that each of the methods yielded similar damping and frequency estimates for the typical section responses. In particular, each predicted the same flutter Mach number, $M_f = 11.9$ ($q_f = 1.92 \times 10^6$ Pa). Furthermore, over the range of Mach numbers considered, the ARMA and LSCFM methods predicted the same aeroelastic behavior for both modes. The MBA1 and MBA2 methods, however, were unable to track the behavior of the first mode as the flutter Mach number was approached. Power spectrum plots of the pitch response, shown in Figs. 8a and 8b, reveal that the frequencies coalesced from $11.0 < M < 11.75$, such that only one peak was identifiable at $M = 11.75$ for use with the MBA1 approach. Similar plots of the modal amplitudes in Figs. 8c and 8d illustrate that the dominant frequency (i.e., global maximum of FFT) of the first modal transient shifts from the first modal frequency to the second modal frequency between $M = 10.0$ and $M = 11.0$. Thus, the MBA2 approach tracks only the second mode for $M \geq 11.0$.

The performance of each method as the time record of the response was reduced is illustrated in Fig. 9. For this aeroelastic system, both the ARMA and the LSCFM methods predicted the aeroelastic

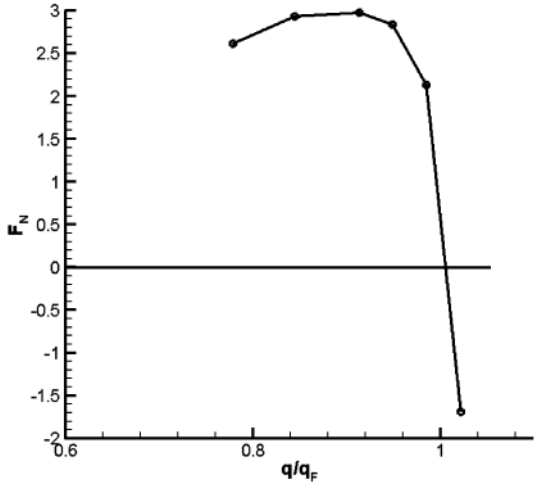

Fig. 13 Flutter margin (FMDS) for a low-aspect-ratio wing using Navier–Stokes aerodynamics, 40,000 ft.

behavior accurately after the time record was reduced substantially. Specifically, the aeroelastic behavior was calculated from these two methods with only 250 time steps, corresponding to 0.06 s of response. Note, however, that the ARMA method required only ~3 s on a 3-GHz Xeon processor to compute system damping and frequencies, whereas the LSCFM required up to 5 min. Thus, in terms of processing efficiency, the ARMA method was superior to the LSCFM. For the MBA1/MBA2 approaches, the flutter Mach number was only slightly reduced; however, the damping and frequency estimates changed significantly when the time record was reduced to 0.25 s (1000 time steps).

The flutter margin for the typical section, computed using Eq. (20), is shown in Fig. 10. As expected, the flutter parameter exhibited a linear variation with dynamic pressure for $0.4q_f < q_\infty < 1.0q_f$. The increase in CAE efficiency due to this parameter is evident when comparing Figs. 7 and 10. The proximity to the flutter point can be easily identified in Fig. 10 using two subcritical aeroelastic responses and a linear extrapolation, whereas in Fig. 7, several responses are required to track the rapid change in modal damping near the onset of flutter. Thus, the binary-mode FMDS reduces the number of aeroelastic transients required to identify flutter and, ultimately, the total cost of the CAE simulation.

IV. Evaluation of the ARMA Approach Using a Multimode Hypersonic Case

The aeroelastic transient responses for the low-aspect-ratio wing case were also generated at 40,000 ft, to again keep the flutter Mach numbers relatively moderate. In a similar analysis to that described earlier, it was determined that 0.125 s (500 time steps) was the minimum amount of response time required to compute damping and frequency estimates.

The damping and frequency characteristics of the low-aspect-ratio wing, estimated using the ARMA and LSCFM methods, is provided in Fig. 11. Note that the damping and frequency estimates were calculated from the displacement of a point at the leading edge of the wing tip. As with the typical section, there is good general agreement between the two methods. However, there was a noticeable difference in the damping estimates for $M = 13.75$ operating condition. This difference resulted in a slightly more conservative flutter Mach number for this case using the LSCFM compared with the ARMA approach. The flutter Mach number was predicted as $M_f = 13.68$ ($q_f = 2.53 \times 10^6$ Pa) and $M_f = 13.58$ ($q_f = 2.50 \times 10^6$ Pa) for the ARMA and LSCFM methods, respectively. Further insight into this difference can be gained by comparing the curve fits of both methods, as shown in Fig. 12. For $12.0 \leq M < 13.75$, the two methods produced excellent curve fits to the transient data. However, at $M = 13.75$, the difference between the actual and LSCFM approximation was noticeable. This result is quantitatively demonstrated by a comparison in the L_∞ norm of the error, as provided in Table 4. Note that the error in the LSCFM fit increases significantly at $M = 13.75$. The L_∞ norm was computed as

$$L_\infty = \max\left(\frac{|w_{\text{actual}} - w_{\text{approx}}|}{\max(|w_{\text{actual}}|)}\right) \tag{30}$$

The flutter margin for the low-aspect-ratio wing, computed using Eq. (23), is shown in Fig. 13. Unlike the typical section system, in which the flutter parameter was linear with dynamic pressure, the multimode system exhibited a nonlinear variation with dynamic pressure. It is evident from these results that the multimode version of the flutter parameter is not valid for this example. Thus, care must be taken when using the multimode flutter parameter described in [14], because it does not perform as expected for all cases.

V. Conclusions

In time-domain CAE analysis, the selection of the damping, frequency, and flutter-boundary identification method has a substantial impact on computational costs. Although the identification methods discussed here produce similar results for the aeroelastic behavior of the systems examined, the ARMA method is superior to both the MBA and LSCFM methods. The ARMA method efficiently produces reliable damping and frequency estimates using relatively short response-time records. Furthermore, in the case of a binary-mode typical section, the ARMA approach can be used to construct a flutter margin that varies linearly with dynamic pressure, minimizing the number of aeroelastic response calculations required for flutter-boundary identification. However, the multimode version of the FMDS does not perform as expected for the case presented in this study. Thus, additional research is required to fully develop the ARMA approach to provide minimum effort flutter-boundary identification of any system.

Acknowledgments

The authors wish to express their gratitude to NASA Langley Research Center for the CFL3D code and thank R. Bartels and Biedron for their help in using this code. This research was funded by the Space Vehicle Technology Institute under grant NCC3-989, jointly funded by NASA and the Department of Defense within the NASA Constellation University Institutes project, with Claudia Meyer as the project manager.

References

[1] McNamara, J. J., and Friedmann, P. P., "Aeroelastic and Aerothermoelastic Analysis of Hypersonic Vehicles: Current Status and Future Trends," 14th AIAA/AHI Space Planes and Hypersonic Systems and Technologies Conference, Canberra, Australia, AIAA Paper 2006-8058, 2006.

[2] Zimmerman, N. H., and Weissenburger, J. T., "Prediction of Flutter Onset Speed Based on Flight Testing at Subcritical Speeds," *Journal of Aircraft*, Vol. 1, No. 4, 1964, pp. 190–202.

[3] Hammond, C. E., and Dogget, Jr. R. V., "Determination of Subcritical Damping by Moving-Block/Randomdec Applications," *Flutter Testing Techniques*, NASA Scientific and Technical Information Office, Washington, D.C., Oct. 1975, pp. 59–76.

[4] Bousman, W. G., and Winkler, D. J., "Application of the Moving-Block Analysis," *Proceedings of the AIAA Dynamics Specialist Conference*, AIAA, New York, 1981, pp. 755–763; also AIAA Paper 81-0653.

[5] Smith, C. B., and Wereley, N. M., "Linear and Nonlinear Damping Identification in Helicopter Rotor Systems," AIAA Paper 98-2003, 1998.

[6] Zhao, Y., and Wereley, N. M., "Time Domain Damping Identification in Helicopter Rotor Systems," 42th AIAA/ASME/ASCE/AHS/ ASC Structures, Structural Dynamics and Materials Conference, Seattle, WA, AIAA Paper 2001-1536, 2001.

[7] Bennett, R. G., and Desmarais, R., "Curve-Fitting of Aeroelastic Transient Response Data with Exponential Functions," NASA SP-415, Oct. 1975, pp. 43–58.

[8] Onoda, J., "Estimation of Dynamic Characteristics of a Wing from the Random Response to Turbulence," *Journal of the Japan Society for Aeronautical and Space Sciences*, Vol. 26, Dec. 1978, pp. 649–656 (in Japanese).

[9] Matsuzaki, Y., and Ando, Y., "Estimation of Flutter Boundary from Random Responses due to Turbulence at Subcritical Speeds," *Journal of Aircraft*, Vol. 18, No. 10, 1981, pp. 862–868.

[10] Wendler, B. H., "Near-Real-Time Flutter Boundary Prediction from Turbulence Excited Response," AIAA Paper 83-0814, 1983.

[11] Batill, S. M., Carey, D. M., and Kehoe, M. W., "Digital Time Series Analysis for Flutter Test Data," *Proceedings of the AIAA Dynamics Specialist Conference*, AIAA, Washington, D.C., 1992, pp. 215–223; also AIAA Paper 92-2103.

[12] Pak, C. G., and Friedmann, P. P., "New Time Domain Technique for Flutter Boundary Identification," *Proceedings of the AIAA Dynamics Specialist Conference*, AIAA, Washington, D.C., 1992, pp. 201–214; also AIAA Paper 92-2102.

[13] Torii, H., and Matsuzaki, Y., "Flutter Margin Evaluation for Discrete-Time Systems," *Journal of Aircraft*, Vol. 38, No. 1, 2001, pp. 42–47.

[14] Bae, J., Kim, J., Lee, I., Matsuzaki, Y., and Inman, D., "Extension of Flutter Prediction Parameter for Multimode Flutter Systems," *Journal of Aircraft*, Vol. 42, No. 1, 2005, pp. 285–288.

[15] Matsuzaki, Y., and Torii, H., "Flutter Boundary Prediction of an Adaptive Smart Wing during Process of Adaptation Using Steady-State Response Data," 47th AIAA/ASME/ASCE/AHS/ ASC Structures, Structural Dynamics and Materials Conference, Newport, RI, AIAA Paper 2006-2132, 2006.

[16] Peloubet, R. P., Haller, R. L., and Bolding, R. M., "On-Line Adaptive Control of Unstable Aircraft Wing Flutter," *Proceedings of the 29th IEEE Conference on Decision and Control*, Inst. of Electrical and Electronics Engineers, New York, 1990, pp. 643–651; also .

[17] Lind, R., "Flight-Test Evaluation of Flutter Prediction Methods," *Journal of Aircraft*, Vol. 40, No. 5, 2003, pp. 964–970.

[18] Jury, I. E., *Theory and Application of the z-Transform Method*, Wiley, New York, 1964.

[19] McNamara, J., "Aeroelastic and Aerothermoelastic Behavior of Two and Three-Dimensional Surfaces in Hypersonic Flow," Ph.D. Thesis, Univ. of Michigan, Ann Arbor, MI, 2005.

[20] Thuruthimattam, B. J., "Fundamental Studies in Hypersonic Aeroelasticity Using Computational Methods," Ph.D. Thesis, Univ. of Michigan, Ann Arbor, MI, 2005.

[21] Thuruthimattam, B. J., Friedmann, P. P., McNamara, J. J., and Powell, K. G., "Aeroelasticity of a Generic Hypersonic Vehicle," 43rd AIAA/ASME/ASCE/AHS Structures, Structural Dynamics and Materials Conference, Denver, CO, AIAA Paper 2002-1209, 2002.

[22] Thuruthimattam, B. J., Friedmann, P. P., McNamara, J. J., and Powell, K. G., "Modeling Approaches to Hypersonic Aeroelasticity," *IMECE2002: 2002 ASME International Mechanical Engineering Congress and Exposition* [CD-ROM], American Society of Mechanical Engineers, New York, 2002; also American Society of Mechanical Engineers Paper IMECE2002-32943.

[23] Thuruthimattam, B. J., Friedmann, P. P., McNamara, J. J., and Powell, K. G., "Modeling Approaches to Hypersonic Aerothermoelasticity with Application to Reusable Launch Vehicles," 44th AIAA/ASME/ASCE/AHS Structures, Structural Dynamics and Materials Conference, Norfolk, VA, AIAA Paper 2003-1967, 2003.

[24] McNamara, J. J., Thuruthimattam, B. J., Friedmann, P. P., Powell, K. G., and Bartels, R. E., "Hypersonic Aerothermoelastic Studies for Reusable Launch Vehicles," 45th AIAA/ASME/ASCE/AHS Structures, Structural Dynamics and Materials Conference, Palm Springs, CA, AIAA Paper 2004-1590, 2004.

[25] McNamara, J. J., Friedmann, P. P., Powell, K. G., Thuruthimattam, B. J., and Bartels, R. E., "Three-Dimensional Aeroelastic and Aerothermoelastic Behavior in Hypersonic Flow," 46th AIAA/ASME/ASCE/AHS Structures, Structural Dynamics and Materials Conference, Austin, TX, AIAA Paper 2005-2175, 2005.

[26] Krist, S. L., Biedron, R. T., and Rumsey, C. L., "CFL3D User's Manual (Version 5.0)," NASA TM-1998-208444, 1998.

[27] Bartels, R. E., Rumsey, C. L., and Biedron, R. T., "CFL3D Version 6.4—General Usage and Aeroelastic Analysis," NASA TM-2006-214301, 2006.

[28] Bartels, R. E., "Mesh Strategies for Accurate Computation of Unsteady Spoiler and Aeroelastic Problems," *Journal of Aircraft*, Vol. 37, No. 3, 2000, pp. 521–525.

[29] Robinson, B. A., Batina, J. T., and Yang, H. T., "Aeroelastic Analysis of Wings Using the Euler Equations with a Deforming Mesh," *Journal of Aircraft*, Vol. 28, Nov. 1991, pp. 778–788.

[30] Cunningham, H. J., Batina, J. T., and Bennett, R. M., "Modern Wing Flutter Analysis by Computational Fluid Dynamic Methods," *Journal of Aircraft*, Vol. 25, No. 10, 1989, pp. 962–968.

[31] Bisplinghoff, R. L., Ashley, H., and Halfman, R. L., *Aeroelasticity*, Addison Wesley Longman, Reading, MA, 1955.

E. Livne
Associate Editor